High absorptivity nanotextured powders for additive manufacturing

O. A. Tertuliano, P. J. DePond, A. C. Lee, D. Doan, X. W. Gu, M. J. Matthews, W. Cai, A. J. Lew

July 26, 2022

Science Advances

MATERIALS SCIENCE

High absorptivity nanotextured powders for additive manufacturing

Ottman A. Tertuliano[1,2]*†, Philip J. DePond[2,3]†, Andrew C. Lee[4], Jiho Hong[4], David Doan[2], Luc Capaldi[1], Mark Brongersma[4], X. Wendy Gu[2], Manyalibo J. Matthews[3], Wei Cai[2], Adrian J. Lew[2]*

The widespread application of metal additive manufacturing (AM) is limited by the ability to control the complex interactions between the energy source and the feedstock material. Here, we develop a generalizable process to introduce nanoscale grooves to the surface of metal powders which increases the powder absorptivity by up to 70% during laser powder bed fusion. Absorptivity enhancements in copper, copper-silver, and tungsten enable energy-efficient manufacturing, with printing of pure copper at relative densities up to 92% using laser energy densities as low as 83 joules per cubic millimeter. Simulations show that the enhanced powder absorptivity results from plasmon-enabled light concentration in nanoscale grooves combined with multiple scattering events. The approach taken here demonstrates a general method to enhance the absorptivity and printability of reflective and refractory metal powders by changing the surface morphology of the feedstock without altering its composition.

INTRODUCTION

Metal additive manufacturing (AM) has widespread potential in the health care, aerospace, automotive, and energy industries (*1*). To date, the application of metal AM is constrained by a small library of weldable materials which can be reliably printed without extensive postprocessing, e.g., stainless steels, AlSi10Mg, some Ni superalloys, and Ti alloys (*2*). These materials are readily printable in commercial laser powder bed fusion (LPBF) systems which typically use a near-infrared (1060- to 1080-nm wavelength) laser to scan over a layer of metal powder to induce melting and fuse the powders. Repeating this process layer by layer results in net shape three-dimensional (3D) printed structures. However, free-form printing of difficult-to-weld high reflectivity and refractory metals has been limited by the photothermal properties of the powder feedstocks (*3*, *4*).

Unlike the aforementioned weldable metals, the low absorptivity (high reflectivity) in the near-infrared and high thermal diffusivity of copper, silver, and their eutectic alloy make localizing heat during laser scanning challenging. Similar obstacles are encountered in LPBF of other high-reflectivity metals (*3*) and illustrate a general need to control the in situ photothermal properties and melting of powders during LPBF. Refractory metals like tungsten also have high thermal conductivities coupled with high melting points that pose further obstacles to AM (*4*, *5*). Because of their high melting points, refractory metals experience large thermal gradients during LPBF that result in residual stresses and cracking after solidification (*6*). Fundamentally changing the interaction of powder feedstock with the energy source to improve absorptivity will expand the library of printable materials to include high reflectivity and refractory metals like copper, silver, and tungsten.

To date, approaches to enable newly printable metals have focused on changing their solidification and recrystallization with engineering solutions that use additives. Adding nanoparticle inoculants to Al 7075 powder enabled printing of high-strength, crack-free structures (*7*). It has been reported that adding copper to Ti enabled forming ultrafine-grained alloys with tunable strength (*8*). A tailor-designed alloy, with functional Fe19Ni5Ti, was developed to produce Damascus steel using LPBF (*9*). Tantalum and rare earth elements are added to tungsten to bind traces of oxygen and mitigate cracking (*10*–*12*).

To specifically improve absorbed laser power, instrumentation is often modified to demonstrate printing of pure copper. High power infrared LPBF systems have been custom built to overcome the low absorptivity barrier, using laser powers of 800 W and higher (*11*, *13*, *14*). These high power systems are reported to damage optical components, are not considered viable solutions (*15*), and must also address the problem that the absorptivity of copper increases with temperature (*16*). This increase makes controlling energy deposition into the copper melt pool difficult, an issue which escalates quickly at ~1-kW laser powers (*14*). Systems with high-powered green lasers are being developed to take advantage of higher absorptivity of copper in the visible wavelengths (*17*), but this can be prohibitively expensive for democratizing AM. For managing detrimental temperature gradients, preheating is more commonly used, specifically with refractory metals (*18*); however, these techniques may require substrate preheating up to 1000°C, and have proved most efficient with high energy density electron beam systems (*19*).

Beyond using high power systems to increase absorbed energy, adding nanoparticles to metal powders has been established as a promising approach to enable the printing of various metals (*7*, *15*, *20*–*22*). High purity copper and copper alloys have been printed by using nanoparticle-decorated copper surfaces (*15*, *21*). These approaches demonstrated that the room temperature optical absorptivity of the decorated copper powder increases to ~60% in comparison to ~20% for the uncoated copper. The use of additives in printing copper has also resulted in reduced electrical conductivity when chromium nitride was introduced to the surface copper powders (*21*) or solidification cracking when carbon nanoparticles are introduced (*15*). The cracks observed in those studies originated at boundaries of segregated additives that did not melt, even at 0.1% weight fraction.

---

[1]Mechanical Engineering and Applied Mechanics, University of Pennsylvania, 220 S. 33rd St., Philadelphia, PA 19104, USA. [2]Mechanical Engineering, Stanford University, 452 Escondido Mall, Stanford, CA 94305, USA. [3]Materials Science Division, Lawrence Livermore National Laboratory, 7000 East Ave, Livermore, CA 94550, USA. [4]Materials Science and Engineering, Stanford University, 496 Lomita Mall Suite 102, Stanford, CA 94305, USA.
*Corresponding author. Email: oat@seas.upenn.edu (O.A.T.); lewa@stanford.edu (A.J.L.)
†These authors contributed equally to this work.

Graphene nanoflakes added to copper at similar weight fractions have resulted in increased absorptivity and relative density of printed parts (*23*). Others have also achieved energy absorption through management of oxide layer on spent powders. Chemical etching of the oxide layer on spent powders has been demonstrated to recover absorption similar to that of unspent powders (*24*). These previous etching approaches primarily aimed to achieve extension of powder lifetime through etching of oxides (*25*). While all the aforementioned processes have opened up avenues of microstructural and photothermal control of powders, to date, no process exists which modifies powder feedstock without alloying or using additives and yet results in improved powder absorptivity, powder dynamics, or print quality of difficult-to-weld high reflectivity and refractory metals.

In this study, we developed an etching process for producing modified metal powder feedstock and, specifically, for improving absorptivity. The surface of conventional metal powders is modified using a wet chemical etching technique to produce nanoscale surface features. We demonstrate an increase in absorptivity, due to an increased localized absorption on the powder's nanoscale features using in situ calorimetry experiments, electromagnetic (EM) simulations on single powder particle surfaces, and ray tracing simulations on a powder bed. Although the quality of printed parts is influenced by many factors beyond absorptivity, we demonstrate that these surface modified powders can enable printing of high purity copper and tungsten metal structures using lower power (100 to 500 W) laser-based metal 3D printing systems. The approach developed here enables printing of difficult-to-weld high reflectivity and refractory pure metals with the same energy requirements as commercially printed alloys.

RESULTS

Etching produces nanoscale surface structures

We produced nanotextured copper, copper-silver, and tungsten powders via a batch solution process. We developed nanotextured copper powders by etching as-purchased (LPW Technology Ltd., 99.95% purity) and as-fabricated [Lawrence Livermore National Laboratories (LLNL), 99.99% purity] copper powders using a solution of $FeCl_3$, HCl, and ethanol (Materials and Methods and fig. S1). The results here are primarily reported for the LPW copper powder with consistent results for the LLNL powder reported in the Supplementary Materials. The as-purchased LPW powder was processed for etch times ranging from 1 to 10 hours (Fig. 1A) to produce powders with varying surface structures. As shown in the scanning electron microscopy (SEM) image in Fig. 1B, the surface of the as-purchased powder initially appeared smooth. After 1 hour of etching (Fig. 1C), the powder began to exhibit uniform roughness on the surface. Figure 1D shows that etching for 5 hours results in surface structures with substantially etched grain boundaries in addition to the uniformly etched grain surfaces observed after 1 hour. This is likely due to a high etching selectivity of grain boundaries. Figure 1E reveals that after etching for 10 hours, grain boundaries became highly visible, and cubic structures with characteristic dimensions on the order of 100 nm on the surface of the powders emerge on the surfaces. Figure 1 (F to I) shows magnified regions of the surface of the powder particles shown in Fig. 1 (B to E), respectively. These magnified images show progressively rougher surfaces characterized by an increase in feature size with etching time up to 5 hours.

We hereon refer to the four powder types based on the etching time as follows: Cu00, Cu01, Cu05, and Cu10, where Cu*X* indicates *X* hours of etching. A similar etching procedure and nomenclature are used for AgCu (Fig. 1, J, K, N, and O) and W powders (Fig. 1, L, M, P, and Q; see Materials and Methods). These results demonstrate the generalizability of the powder etching procedure to high reflectivity and refractory metals.

We quantified the etching by calculating the effective volumetric etch rate using the Cu05 nanotomography results shown in Fig. 1A. The results show tomography of a Cu05 powder particle from two different points of view. By comparing the volume of the etched powder particle to that of its convex hull (fig. S2), we estimated an effective volumetric etch rate of 11 μm^3/hour.

For the specific powder particle measured, we calculated an effective surface depth etch rate of about 71 nm/hour for up to 5 hours of etching. This would be considered a lower bound as we do not account for uniform etching. Further details are provided in the Supplementary Materials.

Nanotextured surfaces increase powder absorptivity

Calorimetry experiments conducted at a laser power of 175 W and a $1/e^2$ beam diameter of 60 μm revealed an improved absorptivity in the nanotextured powders over the as-purchased powders (Fig. 2, A and B) for all materials here. We measured the effective absorptivity, A_{eff}, of the Cu00 powder to be 0.172 at scanning speed 100 mm/s and 0.219 at a scanning speed of 656 mm/s.

At the slower speed of 100 mm/s, the etched powders exhibit improved absorptivities of 0.292, 0.286, and 0.272 for Cu01, Cu05, and Cu10, respectively. At the faster scanning speed of 656 mm/s, we measured the corresponding absorptivities of 0.272, 0.372, and 0.278 for the etched powders.

At both scanning speeds, the nanotextured powders exhibited an absorptivity enhancement factor (absorptivity normalized by that of as-purchased powder absorptivity) of up to 1.7. The Cu05 powder at the faster scan speed provides the highest absorptivity overall. These results are summarized in table S1. We demonstrated similar improvement in absorptivity (enhancement factor of 1.5) using the higher purity LLNL copper powder (fig. S7). AgCu and W demonstrate absorptivity enhancement factors up to 1.3, with W increasing from 0.45 to 0.58 (Fig. 2B).

To gain a better understanding of how nanotexturing enhanced absorptivity on an individual powder particle, we performed EM wave simulations of light absorption on a nanotextured planar surface (see Materials and Methods). The surface profile was extracted from the cross section of the reconstructed Cu powder particle tomograph (Fig. 2C). The higher total absorptivity of the etched powders results from enhanced light-matter interaction on the textured Cu surfaces.

For a 1070-nm wavelength incident plane wave with transverse magnetic polarization (i.e., electric field in the in-plane directions), the simulated field distributions (Fig. 2, D and E) show that certain grooves in the surface (dashed circles) provide strong near-field intensities and boost local absorption (*26*). This result suggests that only a fraction of the powder area leads to the increased absorption of the textured surface compared to the flat one. This enhanced absorption on a single etched particle occurs over a broad range of incident angles (±60°); it results in an average absorption enhancement factor, i.e., the absorption of nanostructure normalized by that of a flat copper substrate, of 1.8 (fig. S4).

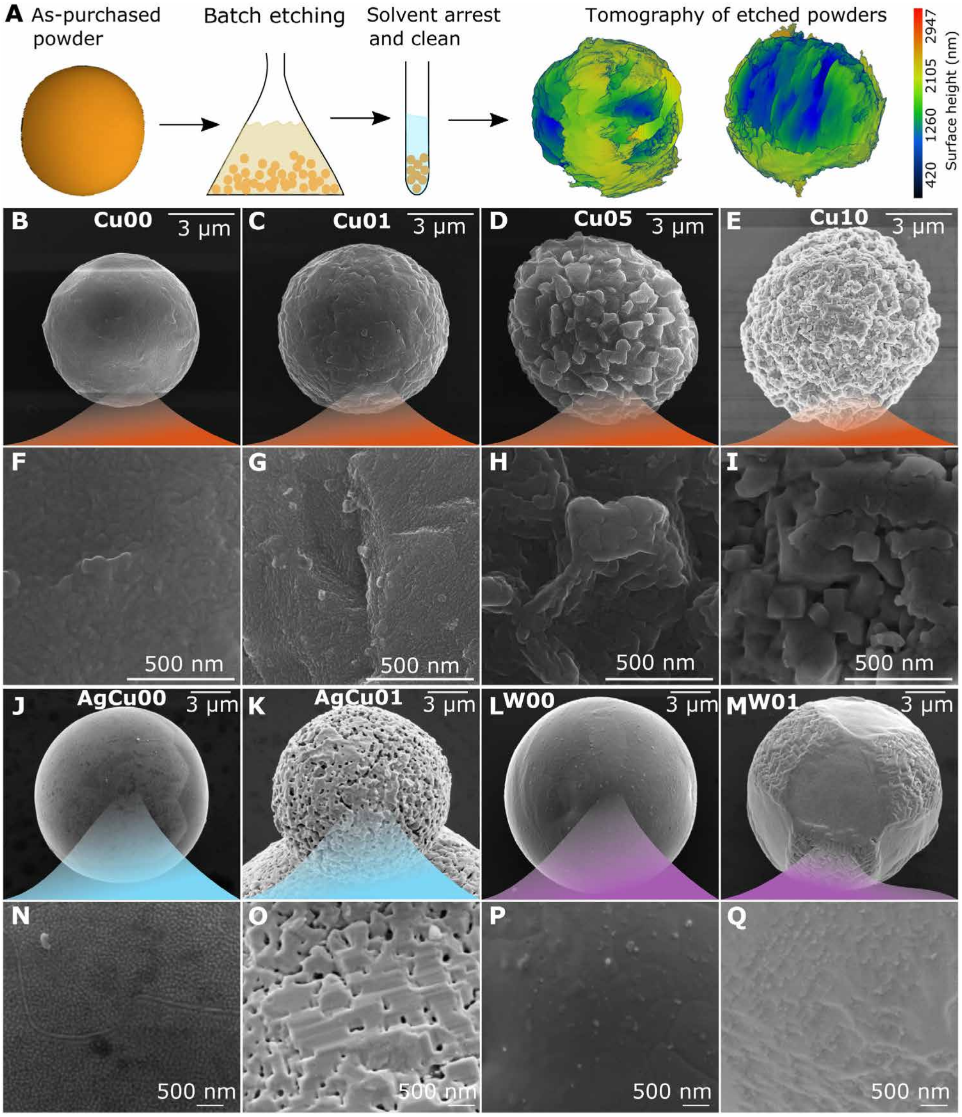

Fig. 1. Surface topography changes of textured powders before and after etching. (**A**) Powder etching procedure with reconstructed 3D images from x-ray nanotomography of etched Cu powder showing surface topography. (**B**) As-purchased (control) powder (Cu00). Powder particles etched for (**C**) 1 hour (Cu01), (**D**) 5 hours (Cu05), and (**E**) 10 hours (Cu10). (**F** to **I**) High-magnification images of powder surfaces showing progressively rougher features characterized by a change in feature size with etching time. Similar results are shown with (J) as-purchased AgCu powder and (K) etched AgCu powder, as well as (L) as-purchased W powder and etched W powder. (**N** to **Q**) High-magnification images of powder surfaces from (**J** to **M**).

To understand how the enhanced absorptivity of a single etched particle affects that of the powder bed, we performed ray tracing simulations on unmelted powder. Informed by the EM simulations, we treat the nanotextured powders as having a fraction of their surfaces, ϕ, with a higher local absorptivity, as shown in Fig. 2F. We simulated powder beds with uniform and bimodal (20 and 40 μm) particle diameter distributions sizes with a 30-μm mean diameter. In each powder bed distribution, we explored the full range of surface area fraction ($\phi \in [0,1]$) with local absorption enhancements factors ranging from 1 to 10.

To check consistency, we calculated the effective absorptivity of untreated Cu00 powders ($\phi = 0$ and an enhancement factor of 1). The predicted absorptivity is 0.240 and 0.176 in the uniform and bimodal diameter distributions, respectively, showing agreement with the measured value of 0.219 (Fig. 2B). Details of the simulation are provided in Materials and Methods.

Figure 2G shows an absorptivity map from simulation results that illustrate possible combinations of ϕ and local enhancement factors for the powders in this work. The iso-absorptivity contours in the same map correspond to the experimental results for 656 mm/s. On the basis of the EM simulations in Fig. 2 (D and E), we expect the etched powders to have low values of ϕ, meaning higher local enhancement factors to enable the same absorptivity on the contour lines of Fig. 2G. The iso-absorptivity contours suggest that the absorptivity is largely determined by and is an increasing function of the product of the local enhancement factor and the surface area fraction. The absorptivity increases faster with this product in bimodally distributed powder than in uniformly distributed powder with the

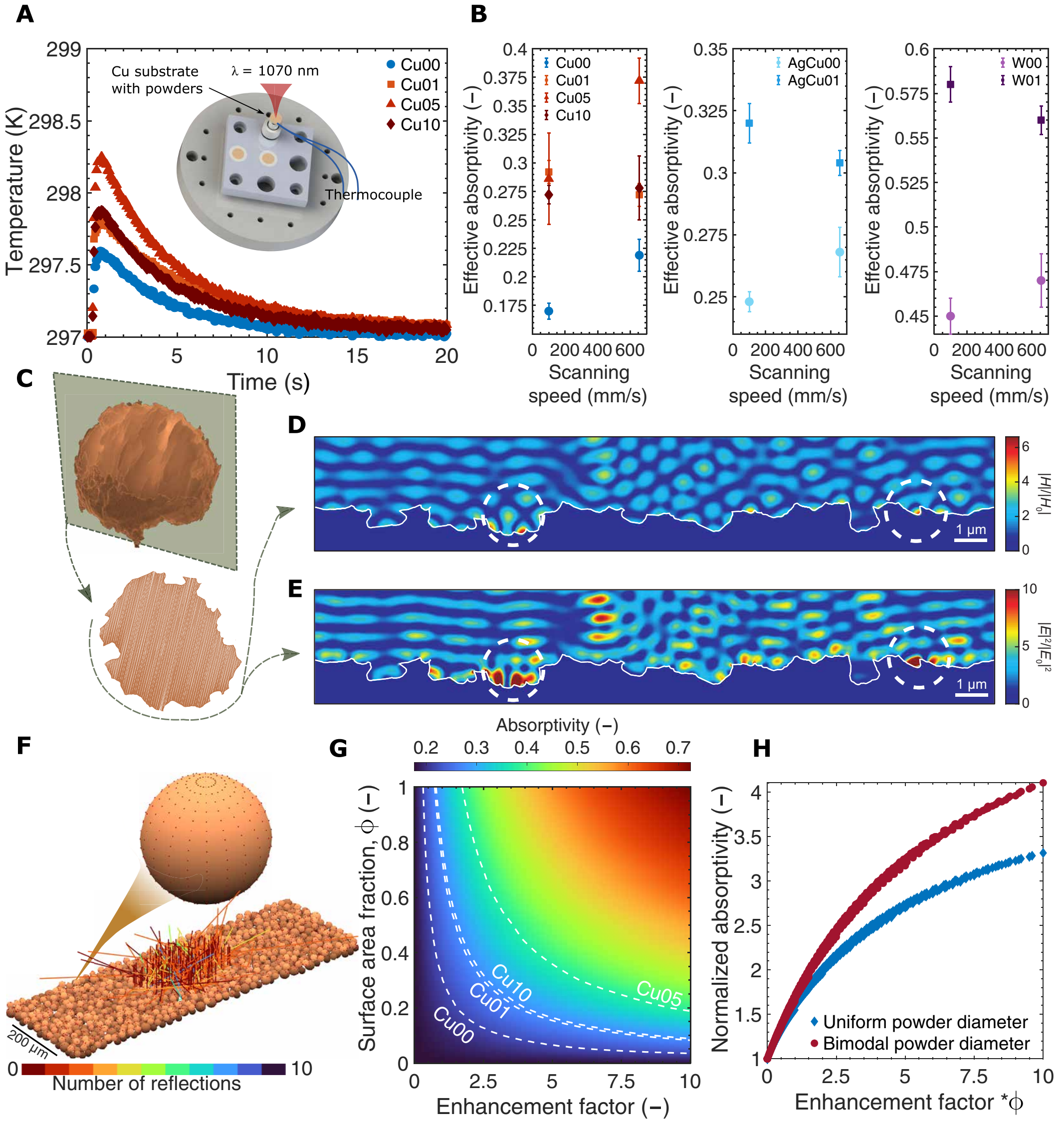

Fig. 2. Experimental and simulated absorptivity enhancement in textured powder. (**A**) Representative time versus temperature data from calorimetry experiments performed at 175 W and 656 mm/s. Data show an increase in peak substrate temperature in etched powder relative to as-purchased powders. Inset shows in situ calorimetry experimental setup. (**B**) Effective absorptivity in as-purchased (blue) and etched copper powders at a laser power of 175 W and two speeds, 100 and 656 mm/s, showing increase in effective absorptivity of etched powder relative to as-purchased copper powders at both scan speeds. Similar results shown for AgCu and W as-purchased and etched powders. (**C**) Sample particle cross section used for EM simulations. (**D**) Normalized magnetic field and (**E**) electric field intensities showing localized fields in surface grooves. (**F**) Representative simulation domain for ray tracing calculations. The colors of the rays represent the number of reflections of each ray, where incident rays are assigned a value of 0. The red spots on the powder particle surfaces indicate regions of enhanced absorptivity, covering a surface area fraction ϕ. (**G**) Absorptivity map from ray tracing simulations of bimodally distributed Cu powder diameter. Dashed lines are iso-absorptivity contours corresponding to the measured absorptivity of Cu powders at 656 mm/s. (**H**) Simulation results showing that absorptivity improves faster in bimodally distributed powders than in uniformly distributed powder. The absorptivity is normalized by the respective values at ϕ = 0 for each powder distributions.

same average diameter (Fig. 2H). These results demonstrate that the manner in which modulating single particle absorptivity influences powder bed absorption is coupled to the powder bed particle size distribution, presenting a multiscale enhancement mechanism.

Nanotextured powders show improved printing at low powers

To assess the viability of high absorptivity nanotextured powders for LPBF, we printed cylindrical structures. We quantified the relative density (i.e., the solid volume fraction) as a function of the laser scanning parameters consolidated as the volumetric energy density, $Q = \frac{P}{htv}$ (see table S2), where P and v are the laser power and speed, and h and t are the hatch spacing and powder layer thickness. At lowest values of Q (83 J/mm^3, calculated for the scanning condition of $P = 100$ W and $v = 300$ mm/s and $P = 200$ W and $v = 600$ mm/s), the etched powders provided an improvement in relative density over the as-purchased powders (Fig. 3A). At 100 W and 300 mm/s, the print using the Cu10 powders has density of 0.926 with a measurement error of ±0.004 (Fig. 3, A and G), an improvement over the 0.856 ± 0.003 observed in the Cu00 powder (Fig. 3, A and E).

The Cu05 powder demonstrates similar relative density of 0.870 ± 0.005 (Fig. 3, A and F) as the as-purchased powder. Under these conditions, porosity stems primarily from lack-of-fusion defects (Fig. 3, E and F). At the same Q, but with twice the power and speed (200 W and 600 mm/s), the different powders produced similar quality builds with relative densities. As Q was increased beyond 200 J/mm^3, the relative density converged to around 0.98 to 0.99 for all prints regardless of powder treatment. It has been shown that laser-powder interactions become less relevant at high powers (greater than 200 W in stainless steel) because the beam simply resides on top of the melt pool rather than interacting with the powder (*27*). Our results are consistent with that observation as the improvement in print quality is most beneficial at lower energy inputs.

Relative density measurements from tomography of the 100 W printing condition samples, shown in Fig. 3 (B to D), are consistent with those acquired from the SEM images in Fig. 3A. The tomography reveals that at low powers, the nanotextured powders may exhibit more fluctuations in relative density as a function of build height (Fig. 3, L and M), compared to that observed in the as-purchased powder. This suggests that at lower powers, there may be different laser-powder interactions and melt and powder dynamics in these higher absorptivity nanotextured powders relative to the as-purchased powders (*27*). At high powers of 400 W, these differences are less relevant as we observe high relative density prints (Fig. 3A and figs. S8 and S9).

DISCUSSION

Surface nanotexture is self-evolving

The surface morphology results for copper suggest that the powder undergoes three main stages during the etching process: uniform etching, grain boundary etching, and redeposition. We can better understand the powder's evolution through these stages as the etching of Cu in FeCl$_3$ solutions occurs through two reactions. The FeCl$_3$ strips Cu from the powder surface to create CuCl$_2$ in solution. This CuCl$_2$ in solution further acts as a secondary etchant by creating complexes with Cu from the powder surface to create 2CuCl. In a three-stage etching process, uniform etching occurs first in the 1-hour timescale due to dissociation of Cu from the surface by forming complexes with Cl$^-$ ions in the solution. Second, in the 5-hour timescale, grain boundary etching becomes evident, as the etching selectivity of grain boundaries is higher than in the bulk (*28*). This is demonstrated further in supplementary images of Cu05 powder (fig. S11).

The third step occurs when further processing of the powders between the 5 and 10 hours results in redeposition of cubic nanocrystals on the surface of the powder particles, without altering the feedstock composition. Energy dispersive spectroscopy in an SEM has indicated that these nanocrystals are primarily copper (fig. S12). Copper in the etching solution may exist as CuCl$_2$ or 2CuCl, and the nucleation of the observed cubic structures on the powder surface may be energetically favorable in the concentrations achieved before

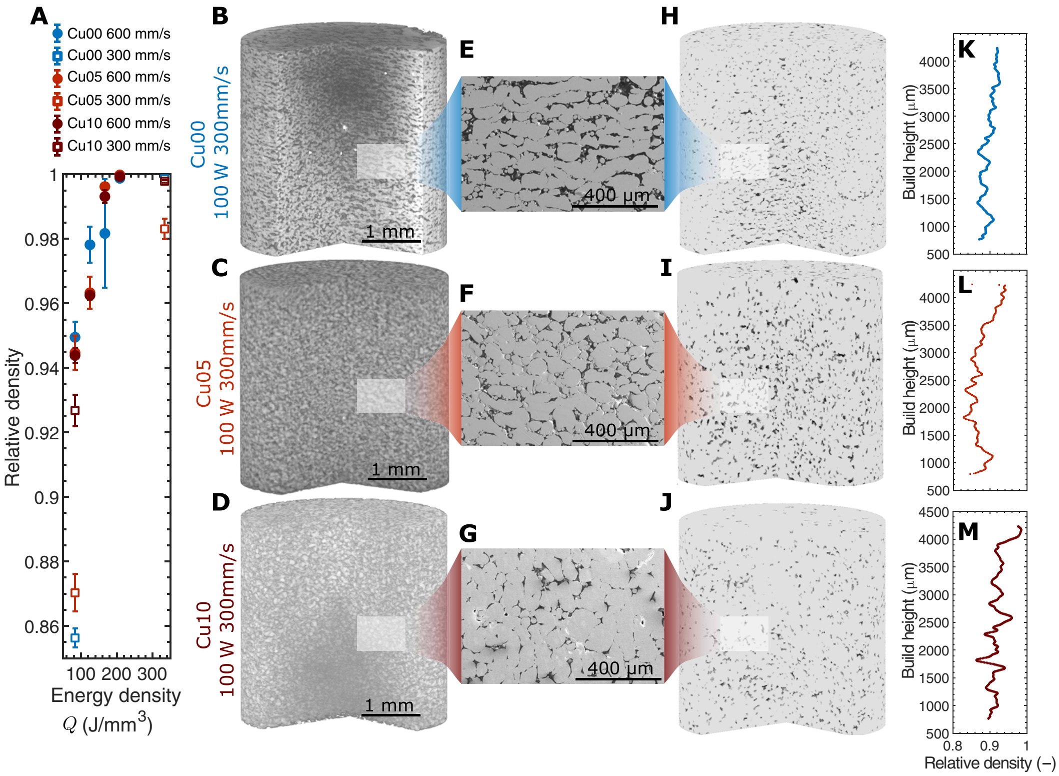

Fig. 3. Relative density and XCT density variations in printed volumes. (**A**) Relative density as a function of volumetric energy density, Q. (**B** to **D**) X-ray computed tomography results of a cylindrical volume extracted from the center of 6-mm cylinder builds for $Q = 83$ J/mm^3. (**E** to **G**) SEM cross sections of builds in (B) to (D), respectively. (**H** to **J**) Binarized tomography results using a watershed scheme. (**K** to **M**) Relative density as a function of build height averaged over 55-μm increments.

10 hours of etching. The Cu nucleates in highly faceted cubic morphology with orthogonal faces, indicating preferential growth of {100} crystal planes, as observed in Fig. 1H. For the observed cubic structures to emerge, two conditions should have been met in the etching solution: (i) The solubility limit of 2CuCl in the diluted HCl (~5 g/100 ml) should have been reached, and (ii) there should be a preferred dissociation of Cu from Cl such that Cu crystals can nucleate and grow on Cu powder surfaces. Using the volumetric etch rate of 11 μm^3/hour from the single particle nanotomography, we estimate that 100 g of powder with a mean particle diameter of 30 μm dissolves at about 86 mg/hour. This results in about 0.86 g of Cu available to create 1.3 g of CuCl in the 100 ml of etching solution in 10 hours of etching. This amount of CuCl is consistent with the solubility limit in HCl, within an order magnitude, and supports redeposition as a mechanism of creating the cubic structure observed on the Cu10 powders (Fig. 1I). Thus, etching to produce surface features characteristic of the powder grain structure requires either a shorter time (e.g., 5 hours in this work) or dilute enough solution in active species to prevent renucleation.

Self-evolved surface nanotexture modifies in situ laser-powder interactions

The measured absorptivity of the all nanotextured powders increases relative to that of all the as-purchased powders under all etching conditions. Previous efforts aimed at improving absorptivity of powders in LBPF involve reducing average powder size (*29*, *30*), alloying (*22*), or using additives (*15*, *23*). These methods have inherent limitations in powder handling and chemical composition. Our results demonstrate the ability to alter absorptivity of metal powder feedstock, using surface topography, without changing composition. The concept of using nanoscale topography to modify absorptivity is observed in nature and is a well-explored principle in flat optical devices (*31*–*35*). The approaches used to modify absorptivity of flat surfaces use carefully designed 2D, lithographically generated patterns on substrates to achieve a desired absorptivity or light-matter interaction (*35*, *36*). Lithographic patterning to achieve such surfaces is not easily translatable and scalable to spherical powder surfaces, especially for metal AM. Here, we produce self-evolved nanostructures by leveraging the anisotropic solution-based etching of metallic grains. This strategy enables high-throughput production of powders with improved absorptivity for metal AM.

While all the self-evolved nanotextured powders showed improvements in absorptivity, the Cu05 powder provided the largest absorptivity enhancement under the explored laser scanning conditions. The beam conditions of 175 W and 656 mm/s resulted in a low Q value of 67 J/mm^3 and the highest A_{eff} measured in the Cu05 powder. At such low energy densities applied to copper powder, we expect the laser to interact with fully intact or partially sintered powder rather than a fully formed melt pool (*37*). These lower energy density beam conditions result in the absorptivity being measured in the conduction regime in copper (*23*), where the absorptivity enhancement from multiple reflections in a keyholing regime does not contribute. Modification of powder particle surface geometry is expected to have a larger effect on absorptivity at low energy densities relative to scanning at high power and slow speeds. On the basis of the feature sizes on the powder particle surfaces, we expect that nanoscale grooves provide regions of high absorptivity (*35, 38*).

For nanoscale groove features to efficiently improve absorptivity, the groove dimensions are critical to induce optical or plasmonic resonance and localized heating at the laser wavelength (*39*). The EM simulations on a full surface contour of a single powder particle provide an absorption enhancement factor of 1.8 (fig. S4) that is consistent with the measured value of 1.7. The strong EM fields at the surface are mainly attributed to plasmonic resonances supported by individual grooves (*38, 40*). Understanding the drop in absorption enhancement from Cu05 to Cu10 requires understanding field localization in relation to local groove dimensions on particle surfaces.

We chose representative grooves in the extracted surface profile and performed the EM simulation of each individual groove on a flat surface. The simulated absorption spectrum displays an optical resonance around the laser wavelength used in the experiment (fig. S5). On resonance, the simulated field distributions show large field magnitudes inside the groove and along the air-Cu interface, similar to those of the entire extracted surface profile. Because of its relatively low optical quality factor (fig. S5C), the plasmonic resonances supported by the grooves also display a broad angular response (*35*). Since the general behavior of such resonances depends on the dimensions of the resonator, simple rectangular grooves can provide similar mode profiles and spectral responses to those of experimentally extracted ones and be used to study the trend of the change in absorption as a function of the etching time. Through parametric sweeps, we observed that the absorption is increased for taller grooves, especially with subwavelength widths (fig. S6). The incident light can funnel into the narrow grooves due to their strong near-field magnitude and be absorbed while propagating along the gap between the sidewalls of the grooves. The in-coupled light can also be reflected at the top and bottom of the grooves, and this gives rise to plasmonic resonances that are mainly governed by the groove height. The Cu10 powder has shallower surface grooves relative to Cu05 (Fig. 1, G and H), due to redeposition of Cu, which can explain the measured drop in absorptivity.

The textured surface also has grooves with large widths, particularly Cu05. Such grooves can support higher-order plasmonic resonance in the lateral direction where the light propagates along the interface between their sidewalls, i.e., surface plasmon resonances (fig. S5). This also further contributes to the higher absorption of Cu05. The numerical analysis corroborates well with the experimental results that the absorption increases from Cu00 to Cu05 and decreases to Cu10.

The overall increase in absorptivity of Cu is larger than that observed in AgCu and W. Our approach to enhancing light absorption by introducing grooves in a metal surface is quite general for high (optical) conductivity of our metal, such as Ag, Cu, and W. However, the absorption is a function of the metal's conductivity as well as the groove dimensions and spatial distribution of the grooves. For each material, the groove properties would require a one-time optimization. The smaller improvement for AgCu and W can be explained by the fact that we have not performed a detailed optimization for these materials. In addition, we found that etching tungsten resulted in a more faceted and globally symmetric nanostructures on the surface of the powders. As a result, the effect of nanotexturing is more subtle with tungsten, from an absorptivity of 0.45 to 0.58 on the powder bed. The absorptivity enhancement on the nanotextured W could come from a variety of mechanisms including localized electric field intensity at sharp facets as well as plasmon modes in any residual tungsten oxide. Unlike the other materials in this study, it has been demonstrated that the oxide of tungsten, WO_2, exhibits a low Q, tunable plasmonic resonance at a wavelength around 1 μm in the near infrared (*41*). The exact mechanism could be investigated in a dedicated study.

Ray tracing simulations suggest that the electric field localization mechanism of absorption enhancement at the nanoscale on particle surfaces may contribute differently to the absorptivity of a powder bed. A parametric study changing ϕ and absorption enhancement factor to match experimentally measured powder bed absorptivities showed the possible combinations of absorption enhancement factors and fractions of surface area contribution to absorption on each powder system (Fig. 2H). Specifically, ray tracing uniquely captures the coupling between particle absorption and powder bed absorption when the particle diameter distribution is altered. We find that we may improve the absorptivity of a nonuniformly (e.g., bimodal here) distributed powder bed at a faster rate than on uniformly distributed powder bed (Fig. 2I) by nanotexturing, i.e., improving single particle absorption (*42, 43*).

Nanotextured powders enable printing

In the explored printing conditions, we observe the highest improvement in print quality using the Cu10 powders, as quantified by relative density measurements. The improvement is most pronounced at low energy densities, at which the surface structure of the powder is expected to play a larger role in light-matter interactions. However, the absorptivity measurements showed that Cu05 has a higher absorptivity than Cu10. The printing quality is influenced by other factors in addition to absorptivity. The higher absorptivity in Cu05 could result in recoil pressure–induced expulsion of powder from the laser path. This could lead to increased denudation or back spatter and may manifest as lack-of-fusion defects observed here (*27*).

The question of how enhanced intrinsic absorptivity of the nanotextured powders can result in improved print quality requires a discussion of how powders are involved after the melt pool as formed. During printing, the laser is most likely incident on the melt pool. However, it is important to note that powders are not fixed in space. Inward flow of entrained powder particles from the denudation zone results in the laser also incident on powder particles during printing. Many of these particles can melt as they get close to the melt pool not only from conduction but also from the incident laser (*44*). There is also a large portion of scattered laser in high reflectivity metals like copper. These scattered rays interact with the particles around the melt pool (*45–47*). High-speed video experiments (*44*) have shown that those powder particles may melt from absorption of scattered rays. This absorption of the scattered laser would also be enhanced by inward flow of powders from the denudation. The present approach may benefit from increased absorptivity of etched powders near the melt pool to improve print quality. The mechanisms by which enhanced powder absorptivity could lead to improved printing (or relative density in this work) can be discussed in the context of work by Khairallah *et al.* (*27*). Those authors demonstrated that particles in front of the laser (spatter, lead powder particles, etc.) can contribute to lack of fusion defects. Increasing power to melt and incorporate those spatter particles into the melt pool was demonstrated as a strategy to minimize such defects. A similar mechanism may occur in our higher absorptivity nanotextured powders but without the use of increased laser power. Determining the specific contributions of the described mechanisms to improved print quality of in the high absorptivity nanotextured powders would require a dedicated experimental and computation study on the powder dynamics.

Despite these current limits in understanding fundamental powder dynamics, we demonstrate the utility of the high absorbing powders by printing structures including 50-mm-long triply periodic minimal surfaces (Fig. 4, C and D, and fig. S10) at a power of 100 W and a scanning speed of 300 mm/s, a result not achievable using conventional, as-purchased copper powder. Figure 4A generally illustrates the accessible processing conditions enabled by the nanotextured powder developed in this work, relative to other approaches or materials (*29, 48–51*). AgCu structures can be printed using slightly higher energy densities (Fig. 2E). It is noteworthy that the use of energy density as a metric here is not to explicitly predict porosity but to provide context to understand the observed changes in print quality with respect to previous studies. The nanotextured powder lowers the required energy densities for printing copper to levels similar to those for stainless steel and Ti alloys.

The print efficacy of the nanotextured powders was also contextualized by accessing the mechanical performance of printed tungsten via nanoindentation in Fig. 4B. Cylinders similar in size to Cu specimens were printed with energy densities ranging from 500 to 1250 J/mm^3. We measure an indentation hardness of ~5 GPa at an energy density of 725 J/mm^3, i.e., a hardness higher than that of other additively manufactured tungsten but achieved at lower energy densities (*12, 52–56*). This energy density can be used to print small octet structures as demonstrated in Fig. 4F. Although the issue of cracking still remains to be solved in the printing of refractory metals, the higher absorptivity powders enable improved constitutive material properties with a fraction of the energy used using other methods.

We demonstrated that the absorptivity of metal powder feedstock can be increased via self-evolving surface texture in an etching solution, without alloying or use of high absorbing nanoparticle additives. We attribute the increased absorptivity to the localization of incident light at nanoscale grooves on the powder surface, where groove dimensions smaller or comparable to the wavelength of the laser lead to resonances. The high absorptivity powders can enable printing starting at low energy densities (83 J/mm^3). These printing conditions have not been previously reported to print copper for the measured relative densities ($\geq$0.92). The powders developed here can be used for printing in moderately powered (~400 W) commercial LPBF systems. These geometrically imperfect powders present a deviation from the idealized, smooth sphere morphology sought after in creating powder feedstock (*57*) yet present an improvement in photothermal efficiency and print quality in manufacturing. Our generalizable approach leverages feedstock surface imperfections to improve the laser-material interdependence without modifying the laser or the material composition.

MATERIALS AND METHODS

Powders

Two copper powders were used in the study. A commercially available copper powder was purchased from LPW/Carpenter Additive (99.95% purity), the results for which are described throughout the main text. A second set of copper powder was obtained from LLNL (99.99% purity). This powder was made at LLNL through gas atomization using C10100 powder stock, and its results are primarily shown in the Supplementary Materials. Eutectic AgCu was purchased from LPW/Carpenter Additive (28.1 wt % Cu and 71.9 wt % Ag). Pure W powder with a mean diameter of 45 μm was purchased from Tekna.

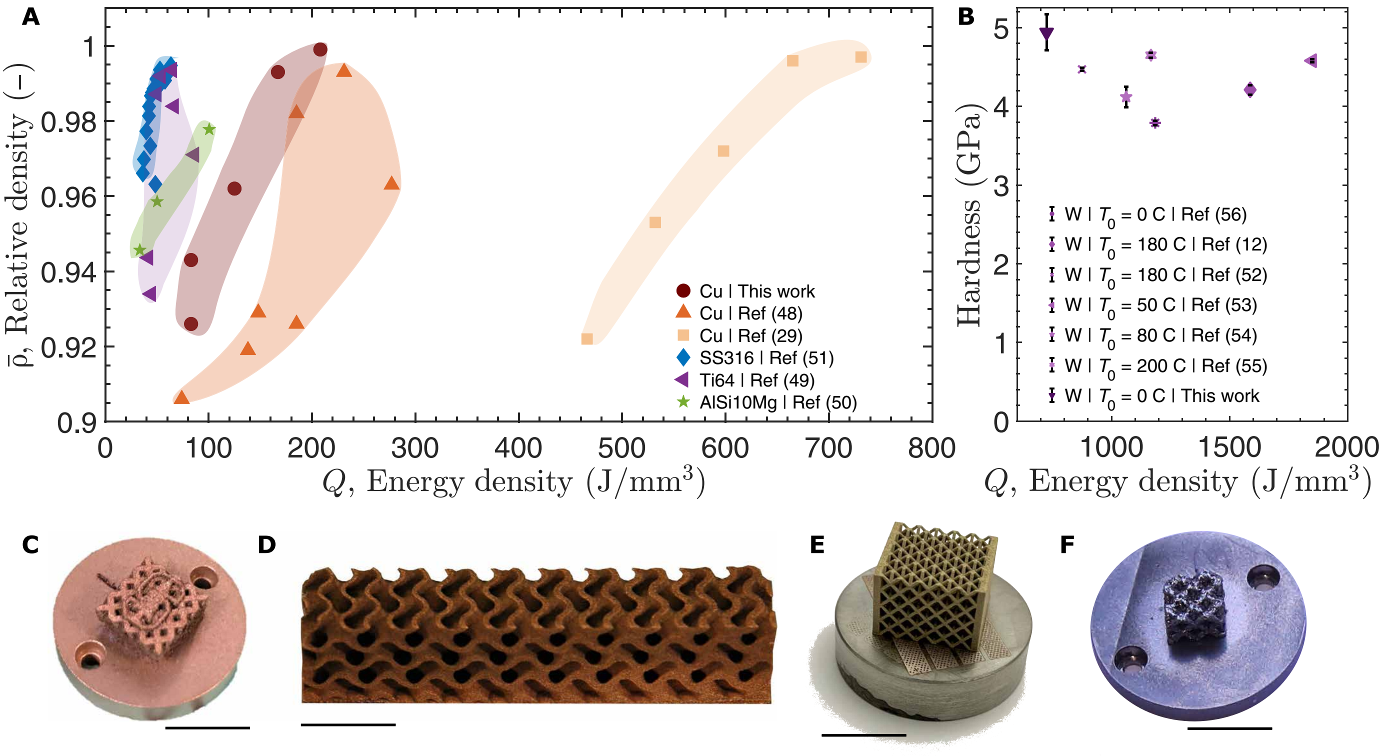

Fig. 4. Low energy density printing of copper and exemplary structures using textured powders. (**A**) Readily printable materials such as SS316, Ti64, and Al alloys are printable with full relative densities ($\bar{\rho} \geq 0.99$) using low energy densities ($Q \leq 80$ J/mm^3). We demonstrate the ability to push the processing conditions of copper to lower energy densities, relative to previous works, using high absorptive Cu05. Shaded areas show qualitative grouping of data. (**B**) Indentation hardness of tungsten cylinder prints contextualized in energy density. The nanotextured W prints result in hardness of ~5 GPa, a value similar to other measurements of additively manufacture pure W, but without the need to preheat powders up to 200 C (see legend). (**C** and **D**) Printing of an octet lattice and a triply periodic minimal surface using Cu05 powders at 87 J/mm^3. (**E**) Octet AgCu printed at 400 J/mm^3. (**F**) Octet W structure printed using W01 at 725 J/mm^3. Scale bars, 10 mm.

Etching powders

To etch the Cu and AgCu powders, we prepared a solution of $FeCl_3$, HCl, and ethanol at a ratio of 70 g:50 ml:150 ml. For 100 g of smooth, as-purchased copper powder (fig. S1, A and B), we first add 25 ml of acetic acid to a 250-ml Erlenmeyer flask and etch the native copper oxide layer on the powder for a total of 5 min, during which the solution turns blue due to the dissolution of the copper oxide layer and distribution of copper (II) ions in the solution; we stir at 400 rpm using a magnetic stir bar for 4 min and subsequently allow the powder to sediment for 1 min. The acetic acid solution is removed from the flask using a pipette, and 100 ml of the $FeCl_3$ etching solution is added to the flask. This solution is covered with paraffin and stirred for 1, 5, or 10 hours at 400 rpm, allowing the powders to be distributed in the solution (fig. S1). The flask is subsequently rested for 5 min without stirring to allow the powder to sediment. The $FeCl_3$ solution is discarded using a pipette. The powder is washed in fresh ethanol eight times (fig. S1D) or until the solution appears clear, by centrifuging in a 50-ml tube at 100 rpm for 60 s. The powders are poured out onto a 150-mm petri dish to dry for 5 hours. After drying, the powders are sieved using <75-μm mesh in a vibratory sieve shaker (FRITSCH ANALYSETTE 3 PRO). The yield from this full process is about 90%, i.e., we produce 90 g of nanotextured powder (fig. S1, E and F) for 100 g of as-purchased powder. This reduced copper mass is a combination of dissolved copper and powder lost from the etching, washing, and sieving processes. The AgCu powder was only etched for 1 hour.

To etch the tungsten powder, we used 30% H_2O_2. For 100 g of as-purchased tungsten powder, we simultaneously add 20 ml of 30% H_2O_2 to a 500-ml Erlenmeyer flask and stir at 600 rpm using a magnetic stir bar. We manually agitate the flask as needed to fully distribute the powders within the acid. Within 2 to 3 min, a reaction proceeds exothermically, releasing water vapor. We allow 5 min for the flask to cool. The liquid that remains is initially light yellow due to soluble tungsten oxide species in solution; upon cooling, the color changes to a characteristic dark blue often associated with the crystallization of tungsten pentoxide. We remove the liquid products with a pipette and repeat the etching procedure for a minimum of three times and a maximum cumulative etching time of 1 hour. The powders are washed, cleaned, and dried similarly to the Cu and AgCu powders.

Absorptivity experiments

To measure the absorptivity of the powders, we built a custom calorimetry experimental setup to fit on the build plate of a commercial metal 3D printer (Aconity Mini 3D). The printer is equipped with a 200-W and 1070-nm Yb-doped fiber laser. Copper substrates of C10100 purity (99.99%) are machined with 2-mm thickness and a recessed area of 4 mm by 4 mm and 50-μm depth. This recessed area is filled with copper powder, and the depth sets the powder layer thickness used in the calorimetry experiments. The laser is then scanned on the powder in the form of a 4-mm line scan. We scan at a power of 175 W and two speeds of 100 and 656 mm/s. At least three experiments are performed per scanning condition for each powder type. During the laser scanning, we collect the temperature of the copper substrate and powder using a type-K thermocouple spot-welded to the back of the substrate. We calculate the absorptivity as the ratio of energy required to raise the sample (powder + substrate) temperature to the measured value relative to the laser energy input from the scanning. The absorptivity measurement and validation are described in detail in previous studies (*23*, *37*).

Printing

We performed all printing experiments using a low-volume, custom built LPBF system at the Advanced Manufacturing Laboratory at LLNL. The metal 3D printing system is equipped with an Yb-doped fiber 1070-nm wavelength scanning laser with a maximum power of 1 kW. The 2.5-cm build plate and approximately 10-mm build height allow for low-volume prints using up to ~200 g of copper powder. For each powder system, 6-mm-diameter cylinders were printed using laser powers ranging from 100 to 500 W and laser scanning speeds of 300 and 600 mm/s. The layer size and hatch spacing were 50 and 80 μm, respectively, for all prints. The build chamber was prepared by pumping to 10^{-3} torr and purging with argon to atmospheric pressure while maintaining an oxygen concentration less than 100 ppm.

Nano and micro x-ray tomography

We performed synchrontron x-ray nanotomography to characterize the surface features and obtain a 3D representation of a single etched powder particle. The experiments were performed at the Stanford Synchrotron Radiation Lightsource (SSRL) Beamline 6-2C. We used a 7-kV beam which produces a 15-nm pixel resolution. The pixels were binned by 2 during image acquisition, resulting in an effective pixel size of 30 nm. Two images are collected (and averaged) at 0.5° increments over a range of 180°. Ten reference images are taken, averaged, and used for background correction in the tomography images. The process and reconstruction are performed using an algebraic reconstruction technique with 20 iterations in TXM Wizard, an open-source software developed at SSRL (*58*). The slices were reconstructed and visualized for surface feature profiling using the software Dragonfly.

We also performed x-ray microtomography to characterize the porosity in the printed cylinder structures using a Sky Scan 1273 x-ray microscope. Pixel sizes range from 4.25 to 5 μm in different scans of the printed cylinders. The slices were reconstructed and visualized for relative density measurements using Dragonfly. Grayscale 3D images were segmented using a watershed transform. Edges between two areas of interest, porous and solid regions, were identified using a Sobel edge detection method. Seeds for areas of interest were manually chosen using histographic segmentation, and a watershed transform enabled segmentation of pores and solid aspects of the prints. Relative density measurements are defined as the volume fraction of the solid regions in the cylinder.

EM wave simulations

EM wave simulations are performed using commercial finite element software (COMSOL Multiphysics) to probe mechanisms of the enhanced optical absorption in nanotextured Cu powder. The actual surface profile of Cu05 powder is extracted from a cross section of reconstructed images acquired via x-ray nanotomography. For parametric studies, the textured powder particle surface is also locally approximated to 2D grooves on a flat and semi-infinite Cu substrate. A normally or obliquely incident plane wave is assumed in the simulations. The absorption enhancement factor is calculated by the ratio of the absorption cross section of the textured surface to that of the flat surface with the same physical area. Optical constants for Cu used in the EM wave simulations are obtained from Palik (*59*). The absorption in the metal is calculated using the following expression of the time averaged power dissipation in Eq. 1

$$W_d = \frac{1}{2}\omega \cdot \mathrm{Im}\{\epsilon\} \int_V |E|^2 \, dV \tag{1}$$

Here, ω is the angular frequency of the incident light, ϵ is the permittivity of the metal, V is the volume of the metal, and E is the local complex electric field.

Ray tracing simulations

COMSOL Multiphysics software and its geometrical optics module were used to perform ray tracing simulations to compute ray trajectories on a powder bed system. It can be used to effectively model EM wave propagation when the ratio of the incident wavelength to the characteristic dimension in the model is less than 0.1 (*60*). While propagating, waves are assumed to be locally plane, and the effects of diffraction at edges and corners in the geometry are typically neglected. We consider beds of as-purchased powder and nanotextured powder in a geometric optics framework. Here, the individual nanotextured powder particles are treated as as-purchased powders but with some fraction of their surfaces ascribed some absorption enhancement factor. To compute ray trajectories, a ray release boundary condition is initialized to specify the initial position and direction of rays. The rays are released from an area with the direction (0, 0, −1) orthogonal to the powder bed. We release 5×10^4 rays with a uniform polarization of (1, 0, 0). Specular reflection boundary conditions are used, such that the angle of incidence (AOI) of the incoming ray matches that of the reflected ray, with respect to the surface normal vector. The classical implementation of Snell's Law and Fresnel equations are used to determine the absorption of the laser at each time step.

As each ray strikes a surface, it absorbed a certain amount. The amount of the ray that is absorbed is a function of its polarization state and AOI with respect to the surface it is striking or nanotextured powder; if a ray strikes a powder surface position designated to have full absorptivity, then it is deactivated.

Supplementary Materials

This PDF file includes:

Supplementary Text
Figs. S1 to S12
Tables S1 and S2
References

REFERENCES AND NOTES

1. T. DebRoy, H. L. Wei, J. S. Zuback, T. Mukherjee, J. W. Elmer, J. O. Milewski, A. M. Beese, A. Wilson-Heid, A. De, W. Zhang, Additive manufacturing of metallic components - Process, structure and properties. *Prog. Mater. Sci.* **92**, 112–224 (2018).

2. S. Liu, Y. C. Shin, Additive manufacturing of Ti6Al4V alloy: A review. *Mater. Des.* **164**, 107552 (2019).
3. T. Q. Tran, A. Chinnappan, J. K. Y. Lee, N. H. Loc, L. T. Tran, G. Wang, V. V. Kumar, W. A. Jayathilaka, D. Ji, M. Doddamani, S. Ramakrishna, 3D printing of highly pure copper. *Metals* **9**, 12–20 (2019).
4. A. Talignani, R. Seede, A. Whitt, S. Zheng, J. Ye, I. Karaman, M. M. Kirka, Y. Katoh, Y. M. Wang, A review on additive manufacturing of refractory tungsten and tungsten alloys. *Addit. Manuf.* **58**, 103009 (2022).
5. P. Morcos, A. Elwany, I. Karaman, R. Arróyave, Review: Additive manufacturing of pure tungsten and tungsten-based alloys. *J. Mater. Sci.* **57**, 9769–9806 (2022).
6. B. Vrancken, R. K. Ganeriwala, M. J. Matthews, Analysis of laser-induced microcracking in tungsten under additive manufacturing conditions: Experiment and simulation. *Acta Mater.* **194**, 464–472 (2020).
7. J. H. Martin, B. D. Yahata, J. M. Hundley, J. A. Mayer, T. A. Schaedler, T. M. Pollock, 3D printing of high-strength aluminium alloys. *Nature* **549**, 365–369 (2017).
8. D. Zhang, D. Qiu, M. A. Gibson, Y. Zheng, H. L. Fraser, D. H. StJohn, M. A. Easton, Additive manufacturing of ultrafine-grained high-strength titanium alloys. *Nature* **576**, 91–95 (2019).
9. P. Kürnsteiner, M. B. Wilms, A. Weisheit, B. Gault, E. A. Jägle, D. Raabe, High-strength Damascus steel by additive manufacturing. *Nature* **582**, 515–519 (2020).
10. J. Xue, Z. Feng, J. Tang, C. Tang, Z. Zhao, Selective laser melting additive manufacturing of tungsten with niobium alloying: Microstructure and suppression mechanism of microcracks. *J. Alloys Compd.* **874**, 159879 (2021).
11. T. T. Ikeshoji, K. Nakamura, M. Yonehara, K. Imai, H. Kyogoku, Selective laser melting of pure copper. *Jom* **70**, 396–400 (2018).
12. Z. Hu, Y. Zhao, K. Guan, Z. Wang, Z. Ma, Pure tungsten and oxide dispersion strengthened tungsten manufactured by selective laser melting: Microstructure and cracking mechanism. *Addit. Manuf.* **36**, 101579 (2020).
13. M. Colopi, L. Caprio, A. Demir, B. Previtali, Selective laser melting of pure Cu with a 1 kW single mode fiber laser. *Procedia CIRP* **74**, 59–63 (2018).
14. M. Colopi, A. G. Demir, L. Caprio, B. Previtali, Limits and solutions in processing pure Cu via selective laser melting using a high-power single-mode fiber laser. *Int. J. Adv. Manuf. Technol.* **104**, 2473–2486 (2019).
15. S. D. Jadhav, S. Dadbakhsh, J. Vleugels, J. Hofkens, P. Van Puyvelde, S. Yang, J.-P. Kruth, J. Van Humbeeck, K. Vanmeensel, Influence of carbon nanoparticle addition (and impurities) on selective laser melting of pure copper. *Materials* **12**, 2469 (2019).
16. B. S. Yilbas, K. Danisman, Z. Yilbas, Measurement of temperature-dependent reflectivity of Cu and Al in the range 30-1000 degrees C. *Meas. Sci. Technol.* **2**, 668–674 (1991).
17. E. Fu, R. Spiegelhalder, S. Vogt, M. Goebel, *Laser 3D Manufacturing IX* , H. Helvajian, B. Gu, H. Chen, Eds. (SPIE, 2022), vol. 1199202, p. 5.
18. A. V. Müller, G. Schlick, R. Neu, C. Anstätt, T. Klimkait, J. Lee, B. Pascher, M. Schmitt, C. Seidel, Additive manufacturing of pure tungsten by means of selective laser beam melting with substrate preheating temperatures up to 1000 C. *Nucl. Mater. Energy* **19**, 184–188 (2019).
19. D. Dorow-Gerspach, A. Kirchner, T. Loewenhoff, G. Pintsuk, T. Weißgärber, M. Wirtz, Additive manufacturing of high density pure tungsten by electron beam melting. *Nucl. Mater. Energy* **28**, 101046 (2021).
20. J. H. Martin, B. Yahata, J. Mayer, R. Mone, E. Stonkevitch, J. Miller, M. R. O'Masta, T. Schaedler, J. Hundley, P. Callahan, T. Pollock, Grain refinement mechanisms in additively manufactured nano-functionalized aluminum. *Acta Mater.* **200**, 1022–1037 (2020).
21. S. D. Jadhav, P. P. Dhekne, S. Dadbakhsh, J. P. Kruth, J. Van Humbeeck, K. Vanmeensel, Surface modified copper alloy powder for reliable laser-based additive manufacturing. *Addit. Manuf.* **35**, 101418 (2020).
22. S. D. Jadhav, D. Fu, M. Deprez, K. Ramharter, D. Willems, B. Van Hooreweder, K. Vanmeensel, Highly conductive and strong CuSn0.3 alloy processed via laser powder bed fusion starting from a tin-coated copper powder. *Addit. Manuf.* **36**, 101607 (2020).
23. O. A. Tertuliano, P. J. DePond, D. Doan, M. J. Matthews, X. W. Gu, W. Cai, A. J. Lew, Nanoparticle-enhanced absorptivity of copper during laser powder bed fusion. *Addit. Manuf.* **51**, 102562 (2022).
24. A. Speidel, L. Gargalis, J. Ye, M. J. Matthews, A. Spierings, R. Hague, A. T. Clare, J. W. Murray, Chemical recovery of spent copper powder in laser powder bed fusion. *Addit. Manuf.* **52**, 102711 (2022).
25. J. W. Murray, A. Speidel, A. Spierings, I. J. Marsh, A. T. Clare, Extending powder lifetime in additive manufacturing: Chemical etching of stainless steel spatter. *Addit. Manuf. Lett.* **3**, 100057 (2022).
26. Y. Qin, X. T. Kong, Z. Wang, A. O. Govorov, U. R. Kortshagen, Near-infrared plasmonic copper nanocups fabricated by template-assisted magnetron sputtering. *ACS Photonics* **4**, 2881–2890 (2017).
27. S. A. Khairallah, A. A. Martin, J. R. I. Lee, G. Guss, N. P. Calta, J. A. Hammons, M. H. Nielsen, K. Chaput, E. Schwalbach, M. N. Shah, M. G. Chapman, T. M. Willey, A. M. Rubenchik, A. T. Anderson, Y. M. Wang, M. J. Matthews, W. E. King, Controlling interdependent meso-nanosecond dynamics and defect generation in metal 3D printing. *Science* **368**, 660–665 (2020).
28. F. W. Young Jr., Etch pits at dislocations in copper. *J. Appl. Phys.* **32**, 192–201 (1961).
29. S. Qu, J. Ding, J. Fu, M. Fu, B. Zhang, X. Song, High-precision laser powder bed fusion processing of pure copper. *Addit. Manuf.* **48**, 102417 (2021).
30. C. Silbernagel, L. Gargalis, I. Ashcroft, R. Hague, M. Galea, P. Dickens, Electrical resistivity of pure copper processed by medium-powered laser powder bed fusion additive manufacturing for use in electromagnetic applications. *Addit. Manuf.* **29**, 100831 (2019).
31. P. Vukusic, J. R. Sambles, Photonic structures in nature. *Bionanotechnology* **424**, 516–537 (2020).
32. N. N. Shi, C. C. Tsai, F. Camino, G. D. Bernard, N. Yu, R. Wehner, Keeping cool: Enhanced optical reflection and radiative heat dissipation in Saharan silver ants. *Science* **349**, 298–301 (2015).
33. T. Shimada, H. Nakashima, Y. Kumagai, Y. Ishigo, M. Tsushima, A. Ikari, Y. Suzuki, What is the key structural parameter for infrared absorption enhancement on nanostructures? *J. Phys. Chem. C* **120**, 534–541 (2016).
34. M. Burresi, L. Cortese, L. Pattelli, M. Kolle, P. Vukusic, D. S. Wiersma, U. Steiner, S. Vignolini, Bright-white beetle scales optimise multiple scattering of light. *Sci. Rep.* **4**, 6075 (2014).
35. T. V. Teperik, F. J. García De Abajo, A. G. Borisov, M. Abdelsalam, P. N. Bartlett, Y. Sugawara, J. J. Baumberg, Omnidirectional absorption in nanostructured metal surfaces. *Nat. Photonics.* **2**, 299–301 (2008).
36. A. Polman, H. A. Atwater, Photonic design principles for ultrahigh-efficiency photovoltaics. *Nat. Mater.* **11**, 174–177 (2012).
37. J. Trapp, A. M. Rubenchik, G. Guss, M. J. Matthews, In situ absorptivity measurements of metallic powders during laser powder-bed fusion additive manufacturing. *Appl. Mater. Today* **9**, 341–349 (2017).
38. T. Søndergaard, S. M. Novikov, T. Holmgaard, R. L. Eriksen, J. Beermann, Z. Han, K. Pedersen, S. I. Bozhevolnyi, Plasmonic black gold by adiabatic nanofocusing and absorption of light in ultra-sharp convex grooves. *Nat. Commun.* **3**, 1–6 (2012).
39. G. Baffou, R. Quidant, Thermo-plasmonics: Using metallic nanostructures as nano-sources of heat. *Laser Photon. Rev.* **7**, 171–187 (2013).
40. V. G. Kravets, F. Schedin, A. N. Grigorenko, Plasmonic blackbody: Almost complete absorption of light in nanostructured metallic coatings. *Phys. Rev. B Condens. Matter. Mater. Phys.* **78**, 97–99 (2008).
41. K. Manthiram, A. P. Alivisatos, Tunable localized surface plasmon resonances in tungsten oxide nanocrystals. *J. Am. Chem. Soc.* **134**, 3995–3998 (2012).
42. C. D. Boley, S. C. Mitchell, A. M. Rubenchik, S. S. Q. Wu, Metal powder absorptivity: Modeling and experiment. *Appl. Opt.* **55**, 6496–6500 (2016).
43. C. D. Boley, S. A. Khairallah, A. M. Rubenchik, Calculation of laser absorption by metal powders in additive manufacturing. *Appl. Opt.* **54**, 2477–2482 (2017).
44. M. J. Matthews, G. Guss, S. A. Khairallah, A. M. Rubenchik, P. J. Depond, W. E. King, Denudation of metal powder layers in laser powder bed fusion processes. *Acta Mater.* **114**, 33–42 (2016).
45. S. A. Khairallah, A. Anderson, Mesoscopic simulation model of selective laser melting of stainless steel powder. *J. Mater. Process. Technol.* **214**, 2627–2636 (2014).
46. P. J. DePond, G. Guss, S. Ly, N. P. Calta, D. Deane, S. Khairallah, M. J. Matthews, In situ measurements of layer roughness during laser powder bed fusion additive manufacturing using low coherence scanning interferometry. *Mater. Des.* **154**, 347–359 (2018).
47. S. A. Khairallah, A. T. Anderson, A. Rubenchik, W. E. King, Laser powder-bed fusion additive manufacturing: Physics of complex melt flow and formation mechanisms of pores, spatter, and denudation zones. *Acta Mater.* **108**, 36–45 (2016).
48. S. D. Jadhav, L. R. Goossens, Y. Kinds, B. V. Hooreweder, K. Vanmeensel, Laser-based powder bed fusion additive manufacturing of pure copper. *Addit. Manuf.* **42**, 101990 (2021).
49. J. J. Dilip, S. Zhang, C. Teng, K. Zeng, C. Robinson, D. Pal, B. Stucker, Influence of processing parameters on the evolution of melt pool, porosity, and microstructures in Ti-6Al-4V alloy parts fabricated by selective laser melting. *Prog. Addit. Manuf.* **2**, 157–167 (2017).
50. N. T. Aboulkhair, N. M. Everitt, I. Ashcroft, C. Tuck, Reducing porosity in AlSi10Mg parts processed by selective laser melting. *Addit. Manuf.* **1–4**, 77–86 (2014).
51. T. Peng, C. Chen, Influence of energy density on energy demand and porosity of 316L stainless steel fabricated by selective laser melting. *Int. J. of Precis. Eng. and Manuf. - Green Tech.* **5**, 55–62 (2018).
52. Z. Xiong, P. Zhang, C. Tan, D. Dong, W. Ma, K. Yu, Selective laser melting and remelting of pure tungsten. *Adv. Eng. Mater.* **22**, 1901352 (2020).
53. C. Tan, K. Zhou, W. Ma, B. Attard, P. Zhang, T. Kuang, Selective laser melting of high-performance pure tungsten: Parameter design, densification behavior and mechanical properties. *Sci. Technol. Adv.Mater.* **19**, 370–380 (2018).
54. P. Rebesan, M. Bonesso, C. Gennari, R. Dima, A. Pepato, M. Vedani, Tungsten fabricated by laser powder bed fusion. *Berg. Hüttenmännische Monatshefte* **166**, 263–269 (2021).
55. M. Guo, D. Gu, L. Xi, H. Zhang, J. Zhang, J. Yang, R. Wang, Selective laser melting additive manufacturing of pure tungsten: Role of volumetric energy density on densification, microstructure and mechanical properties. *Int. J. Refract. Met. Hard Mater.* **84**, 105025 (2019).

56. D. Wang, C. Yu, X. Zhou, J. Ma, W. Liu, Z. Shen, Dense pure tungsten fabricated by selective laser melting. *Appl. Sci.* **7**, 430 (2017).
57. S. Vock, B. Klöden, A. Kirchner, T. Weißgärber, B. Kieback, Powders for powder bed fusion: A review. *Prog. Addit. Manuf.* **4**, 383–397 (2019).
58. Y. Liu, F. Meirer, P. A. Williams, J. Wang, J. C. Andrews, P. Pianetta, TXM-Wizard: A program for advanced data collection and evaluation in full-field transmission X-ray microscopy. *J. Synchrotron Radiat.* **19**, 281–287 (2012).
59. E. Palik, *Handbook of Optical Constants of Solids* (Academic Press, 1985).
60. K. Tang, R. O. Buckius, The geometric optics approximation for reflection from two-dimensional random rough surfaces. *Int. J. Heat and Mass Transf.* **41**, 2037–2047 (1998).
61. L. Landau, E. Lifshitz, *Mechanics*, vol 1. (ed. 1, Pergamon Press; 1960).
62. J. D. Jackson, *Classical Electrodynamics* (Wiley, 1998).

Acknowledgments: We thank T. Pluschkell, J. Fingerle, and M. Ades for providing the LLNL copper powders. We acknowledge US patent application 17/706259 of the invention entitled "Nanotextured metal powders for 3D printing of metals." **Funding:** Part of this work was performed at the Stanford Nano Shared Facilities (SNSF), supported by the National Science Foundation under award ECCS-2026822. Use of the SSRL, SLAC National Accelerator Laboratory, is supported by the US Department of Energy, Office of Science, Office of Basic Energy Sciences under contract no. DE-AC02-76SF00515. Part of this work was performed under the auspices of the US Department of Energy by Lawrence Livermore National Laboratory under contract DE-AC52-07NA27344. We acknowledge funding from National Science Foundation through L.C.'s Graduate Research Fellowship Program (NSF GFRP). **Author contributions:** O.A.T., P.J.D., W.C., and A.J.L. conceived the idea and designed the experiments. O.A.T., P.J.D., A.C.L., D.D., and L.C. performed the experiments. J.H., M.B., and P.J.D. performed simulations. O.A.T. and A.J.L. supervised the project. O.A.T. and P.J.D. wrote the original draft. O.A.T., A.J.L., M.B., X.W.G., M.J.M., and W.C. revised and edited the manuscript. All authors discussed the results and the final manuscript. **Competing interests:** O.A.T., P.J.D., A.C.L., W.C., X.W.G., A.J.L. are inventors on a patent (US patent no. 11938536) held by Stanford University that covers removing material from the surface of the particles using wet chemical etching to create a nanoscale texturing of the surface, increasing absorptivity by the metal powder particles of incident laser light and maintaining flowability. The authors declare that they have no other competing interests. **Data and materials availability:** All data needed to evaluate the conclusions in the paper are present in the paper and/or the Supplementary Materials. Raw data and custom code written to process data in MATLAB are available at doi:10.5061/dryad.3j9kd51td.

Submitted 1 March 2024
Accepted 29 July 2024
Published 4 September 2024
10.1126/sciadv.adp0003